AI-Guided Stability Tuning of a Heterodimeric Linker for Programmable Protein Tube Architectures

Masahiro Noji[1], Takuro Fujiwara[2,3], Yukihiko Sugita[2,4], and Yuta Suzuki[1,5]*

[1]Institute for Integrated Cell-Material Sciences, Kyoto University, Kyoto, Japan; [2]Institute for Life and Medical Sciences, Kyoto University, Kyoto, Japan; [3]Graduate School of Medicine, Kyoto University, Kyoto, Japan; [4]Graduate School of Biostudies, Kyoto University, Kyoto, Japan; [5]PRESTO, JST, Saitama, Japan; *e-mail: suzuki.yuta.2m@kyoto-u.ac.jp

Abstract

The ability to rationally modulate the morphology of artificial higher-order protein assemblies remains limited, particularly for geometrically constrained architectures such as tubes. Here, we show that simple tuning of the interaction stability within a heterodimeric coiled-coil linker, guided by deep-learning-based predictions from ThermoMPNN, provides an effective strategy for programming the assembly behaviour of two-component protein tubes. By engineering a systematic stability gradient within the M3L2/p66α heterodimeric linker, we generated single-amino-acid variants that exhibit predictable shifts in the temperature window for tube formation and produce tubes with distinct diameters. Notably, the least stable variant uniquely accesses multilayered tube-in-tube architectures. Time-course electron microscopy reveals that these hierarchical structures arise through a sequential process involving the initial formation of thin tubes, subsequent wall thickening, and eventual development of nested tubes, highlighting the role of transient linker rearrangements near the thermal transition. Together, these findings establish coiled-coil stability as a minimal and tunable design parameter that governs higher-order morphology and offer a minimal and programmable framework for constructing rationally designed protein tube architectures.

Higher-order protein assemblies underpin a wide range of essential biological processes. Nature employs an extraordinary repertoire of architectures—from cytoskeletal filaments whose length and flexibility are precisely regulated[1-4], to clathrin cages and viral capsids whose size, curvature, and symmetry are carefully controlled[5-8]—to support functions that depend on both structural accuracy and dynamic adaptability. In these systems, morphology is not merely a consequence of assembly but a parameter that is actively tuned to enable transport[2,9], compartmentalisation[10,11], force generation[2,4,12], and responsive behaviour[2,13,14]. Such

naturally evolved mechanisms illustrate a level of morphological control that remains unmatched in artificial protein assemblies.

Transferring these principles into artificial protein design could, in principle, enable the construction of assemblies that are not only geometrically defined but also capable of dynamic, stimulus-responsive behaviour reminiscent of natural systems. Such capabilities would advance both our fundamental understanding of how morphology governs biological function and our ability to engineer artificial structures with the precision and adaptability required for next-generation biotechnological applications[15-20]. Such tunability of morphology may ultimately support applications in which size-defined or compartmentalised architectures are advantageous, including delivery-oriented or catalytic systems. Achieving this goal requires strategies that allow the architecture and physical properties of designed assemblies to be modulated in a predictable and programmable manner.

Recent breakthroughs in computational design have enabled de novo construction of multi-component assemblies[21-24]. Although these computational methods can accurately specify interaction geometries, they provide only limited capacity to adjust the resulting assemblies—such as tuning their size or modulating their overall architecture. Despite emerging platforms that allow modular control over size and shape[25-27], broadly applicable methods for predictably tuning the architecture and mechanical properties of protein assemblies remain relatively scarce. This is particularly true for closed, finite assemblies such as cages and tubes, where geometric constraints impose strict requirements on interaction design.

In our previous work, two-component protein tubes assembled via MBD3L2 (M3L2)/p66α heterodimeric coiled-coil exhibited a broad range of diameters and symmetries, revealing that this system inherently supports rich morphological diversity[28]. This observation suggested that such diversity would be amenable to deliberate tuning through rational design. Building on our previous design philosophy—which integrates naturally inspired heterolinkers with symmetry-defined scaffold proteins to govern assembly pathways—we reasoned that the properties of the coiled-coil linker itself could be exploited as a tunable element to reshape tube morphology. Because the M3L2/p66α coiled-coil serves as the central connecting element of the tube, we hypothesised that subtle modulation of its stability could offer a direct and predictable route to controlling higher-order architecture.

To test this concept, we employed ThermoMPNN, a deep-learning model capable of predicting the stability effects of point mutations with residue-level resolution[29]. This approach allowed us to systematically design point mutations predicted to subtly modulate the stability of the coiled-coil linker without disrupting

heterodimer formation. Moreover, when incorporated into the tube-forming system, these engineered linkers retained assembly competence yet produced distinct morphological outcomes, including increased tube diameters and the emergence of tube-in-tube architectures. Together, these results demonstrate that tuning coiled-coil stability offers a powerful and generalizable strategy for modulating the architecture and dynamics of multi-component protein tubes, thereby expanding the design toolkit for programmable and responsive higher-order assemblies.

Engineering the coiled-coil linker for controlled modulation of tube morphology

Given our observation that the M3L2/p66α coiled-coil linker plays a central role in defining tube morphology, we first sought to test whether intentional modulation of its stability could serve as a design parameter to reshape the architecture of the two-component tubular assemblies (**Fig. 1**).

In our previous study, dynamic rearrangement of the M3L2/p66α interaction near its melting temperature (T_m) facilitated the formation of tubes with diverse diameters and symmetries[28]. This observation suggested that coiled-coil interaction may directly influence assembly pathways and morphological outcomes, making it an attractive target for rational engineering. Because p66α is intrinsically helical and structurally rigid, whereas M3L2 is more flexible and partially disordered[30,31], we focused our engineering efforts on M3L2 while leaving p66α unmodified to avoid disrupting heterodimer formation. Our previous study indicated that morphological diversity of these tubes arises from dynamic rearrangement of the M3L2/p66α interaction near its T_m, where the effective binding strength becomes transiently weakened rather than inherently destabilized. Based on this observation, we introduced a deliberately controlled gradient of stability perturbations into the M3L2 helix to directly test how shifting the coiled-coil's thermal responsiveness governs assembly morphology.

To introduce well-controlled stability perturbations, we systematically designed single-point mutations using ThermoMPNN, a deep-learning model that predicts mutation-induced stability changes ($\Delta\Delta G_{Pred}$) with residue-level resolution[29]. Because ThermoMPNN is not applicable to multimer prediction, we first generated an M3L2-Gly_{50}-p66α heterodimer structure using AlphaFold 2 (AF2)[32], and the most reliable model was used for stability inference (**Fig. 1**). We then confined mutation scanning to previously reported coiled-coil key residues in M3L2[31] and selected 13 point mutations predicted to yield a broad and intentionally destabilised range of $\Delta\Delta G_{Pred}$ values (**Fig. 2a, Table 1, and Supplementary Table 1**). This design strategy ensured that the resulting variant set would span a predictable and tunable spectrum of reduced coiled-coil stabilities.

Having established a set of variants spanning a wide and well-controlled range of predicted coiled-coil stabilities, we next sought to investigate how these mutations affected heterodimer formation with p66α and the thermal behaviour of the resulting coiled-coil complexes. To this end, we first constructed N-terminal His-tagged versions of M3L2 (WT and all mutants) and p66α to characterise their biophysical properties in isolation and in complex.

Expression in *E. coli* yielded both M3L2 and p66α constructs in soluble form, but purification behaviours differed markedly. Whereas 6×His-TEVcs-p66α was readily purified using nickel-affinity chromatography, the corresponding 6×His-TEVcs-M3L2(WT) construct predominantly appeared in the flowthrough, preventing efficient recovery. We therefore extended the His-tag to 8×His-TEVcs, which enabled robust purification of M3L2(WT). All 13 designed variants (Mvs) were subsequently constructed and purified in the same 8×His-TEVcs-tagged format, ensuring consistency across the dataset.

To assess coiled-coil formation between M3L2 and p66α, we performed circular dichroism (CD) spectroscopy using the purified His-tagged peptides (**Fig. 2b and Supplementary Fig. 1**). As expected, M3L2(WT) exhibited a largely disordered conformation, whereas p66α adopted a more helical structure when examined individually. Upon mixing the two peptides, however, a temperature-dependent increase in α-helical signal characteristic of coiled-coil formation was observed, confirming that the isolated peptides can reconstitute the heterodimeric interaction. Although our peptide constructs contain minor sequence differences outside the core coiled-coil region compared with the previously reported peptides, the thermal denaturation profile yielded an averaged T_m ($T_{m,\,Ave}$) of 31.7 °C (**Fig. 2c, Supplementary Fig. 2, Table 1, and Supplementary Table 1**), which is close to the reported value of 34.8 °C for the M3L2/p66α coiled-coil[31]. This agreement indicates that the essential interaction properties of the heterodimer are preserved in our construct and that the purified peptide system reliably recapitulates its expected behaviour.

We next applied the same analyses to the 13 engineered Mvs to determine how the designed stability perturbations influenced coiled-coil formation with p66α. CD spectroscopy revealed that several variants showed reduced or less well-defined coiled-coil signatures, consistent with their strongly destabilising $\Delta\Delta G_{Pred}$. Among the full panel of mutants, five variants—Mv3, Mv4, Mv5, Mv8, and Mv11—formed sufficiently stable coiled-coil complexes with p66α to permit reliable thermal denaturation analysis (**Fig. 2b and Supplementary Fig. 1**).

Thermal unfolding experiments on these five variants yielded well-defined T_m, which collectively spanned a broad and intentionally destabilised range that reflected the designed gradient of reduced coiled-coil

stabilities (**Fig. 2c, Supplementary Fig. 2, Table 1, and Supplementary Table 1**). Importantly, the experimentally obtained $T_{m,Ave}$ values exhibited a strong negative correlation with the ThermoMPNN-predicted $\Delta\Delta G_{Pred}$ values ($r = -0.71 \pm 0.35$), supporting the validity of our deep-learning-based design strategy (**Fig. 2d**). This agreement indicates that ThermoMPNN successfully generated mutations whose experimentally observed effects followed the expected systematic decrease in coiled-coil stability across the engineered spectrum. For the remaining variants, thermal denaturation curves were poorly defined, in line with their weak CD signatures (**Supplementary Figs. 1 and 2**), preventing reliable T_m determination. These observations are consistent with the strongly destabilising $\Delta\Delta G_{Pred}$ values for these mutants and confirm that our engineered M3L2 panel spans a deliberately extended and well-controlled range of coiled-coil stabilities. This set of linkers therefore provides a robust foundation for evaluating how stability tuning influences the morphology and assembly behaviour of the two-component protein tubes.

Structural analysis of engineered coiled-coil variants

To understand how the designed mutations influenced coiled-coil formation with the deliberately constructed stability gradient, we next analysed the structural consequences of each substitution using AlphaFold 3 (AF3)[33]. AF3, which employs a diffusion-based generative approach, has recently been reported to provide improved accuracy for predicting protein–protein interactions and the effects of point mutations relative to AF2[33-35]. We therefore generated AF3 structural models for all M3L2/p66α heterodimer pairs (**Fig. 2e–i and Supplementary Fig. 3**).

Among the variants, Mv1 (Q3Y) had the lowest destabilising $\Delta\Delta G_{Pred}$ (**Supplementary Table 1**), yet the AF3 model suggested that this mutation disrupts an interchain hydrogen bond near the disordered N-terminal region of M3L2 (**Supplementary Fig. 3a**). Although this mutation shows only a small predicted destabilising effect in terms of $\Delta\Delta G$, the reduced reliability of structure prediction within intrinsically disordered regions may obscure additional intra- or interchain contacts, and such unmodelled interactions could inhibit coiled-coil formation.

For Mv2–Mv4, AF3 models indicated that the mutated residues do not directly participate in interchain interactions (**Fig. 2e, f and Supplementary Fig. 3b**). This is consistent with their relatively modest $\Delta\Delta G_{Pred}$ values (**Table 1, Supplementary Table 1**). Nonetheless, Mv2 (P7G) exhibited surprisingly weak coiled-coil propensity in experiments. Because P7 is located at the helix "N-cap," where proline contributes favourably to helix stability[36,37], replacing it with glycine may reduce local structural stability more than predicted, explaining the experimentally observed destabilisation.

169 The remaining variants (Mv5–Mv13) generally weakened or disrupted interchain packing interactions, in
170 agreement with their higher $\Delta\Delta G_{\mathrm{Pred}}$ values (**Fig. 2g–i, Supplementary Fig. 3c–h, Table 1, and**
171 **Supplementary Table 1**). These models support the interpretation that mutations predicted to be highly
172 destabilising by ThermoMPNN indeed perturb key interchain interactions within the coiled-coil interface.
173 Together, these AF3-based structural analyses rationalise the experimentally observed stability gradient
174 across the M3L2 variant panel and reinforce the suitability of computationally guided stability tuning as a
175 foundation for subsequent morphology control in the two-component tube system.
176
177 **Effect of coiled-coil stability tuning on two-component tube formation**
178 Having established that the engineered M3L2 variants span a wide range of coiled-coil stabilities, we next
179 examined how these stability differences influence the morphology of the two-component tubular
180 assemblies (**Fig. 3a**). Because the majority of variants either formed weak or poorly defined coiled-coils
181 with p66α or lacked reliable thermal unfolding behaviour, they were unlikely to yield interpretable
182 outcomes when incorporated into the PuuE system. Among the variants that did form sufficiently well-
183 defined coiled-coils, Mv3 and Mv4 represented the most informative pair: they exhibited the highest and
184 lowest $T_{\mathrm{m,Ave}}$ values, respectively, within the reliably characterised subset, and their $T_{\mathrm{m,Ave}}$ values decreased
185 in an approximately uniform manner across the panel (**Table 1**). These features provided an intentionally
186 broad and predictable contrast in linker stability, allowing us to probe how defined shifts in thermal
187 responsiveness affect assembly morphology. Based on this rationale, we selected Mv3 and Mv4 as
188 representative variants for incorporation into the PuuE system.
189
190 As reported previously[28], PuuE-M(WT) and PuuE-p form two-component tubes via the C-terminal
191 M3L2/p66α coiled-coil linkers, with tube formation being strongly promoted at 35 °C, likely due to thermal
192 fluctuations near the T_{m} of the coiled-coil linker (**Fig. 3b**). This temperature dependence further motivated
193 the use of stability-shifted linkers to modulate assembly outcomes in a controlled manner. To evaluate this
194 possibility, we introduced the Mv3 and Mv4 mutations individually into PuuE-M(WT) and purified the
195 resulting proteins (PuuE-Mvs) to assess their effects on tube assembly (**Fig. 3a**). Both PuuE-Mv3 and PuuE-
196 Mv4 were purified successfully and, when examined in isolation, did not form higher-order structures
197 according to negative-stain transmission electron microscopy (nsTEM) imaging (**Supplementary Fig. 4**).
198 Upon mixing with PuuE-p at 35 °C, PuuE-Mv3 and PuuE-Mv4 formed tubes in a manner broadly similar
199 to the wild-type system (**Fig. 3b, Supplementary Fig. 5**), confirming that both variants retain the minimal
200 requirements for heterodimerisation with p66α and for productive tube assembly. With tube formation
201 established across PuuE-M(WT), PuuE-Mv3, and PuuE-Mv4, we next turned to how differences in coiled-

coil stability influence more detailed aspects of assembly behaviour, including temperature dependence and tube architecture.

To dissect the temperature sensitivity of each linker variant, we examined how the stability differences between Mv3, Mv4, and the WT linker affect the temperature dependence of tube formation. As reported previously[28], the PuuE-M(WT)/PuuE-p system exhibits a strong temperature dependence, with efficient tube formation occurring between 30 and 40 °C and only limited assembly at lower temperatures. This behaviour is attributed to dynamic rearrangements of the M3L2/p66α coiled-coil interaction near its T_m. Consistent with this temperature dependence, mixtures of PuuE-M(WT) and PuuE-p formed micron-scale tubes most efficiently at 35 °C, whereas markedly fewer tubes were observed at 15 °C (**Fig. 3b, Supplementary Fig. 5**). In contrast, the three linkers exhibited a clear stability-dependent continuum: PuuE-M(WT) showed almost no tube formation at 15 °C, PuuE-Mv3 displayed partial but limited assembly, and PuuE-Mv4 retained robust tube-forming capability even under these low-temperature conditions. Notably, PuuE-Mv4—the least stable coiled-coil among the reliably characterised variants—retained substantial tube-forming capability even at 15 °C, producing discernible micron-scale tubes under conditions where both WT and Mv3 showed only sparse assembly. In contrast, PuuE-Mv3, whose coiled-coil stability is intermediate between WT and Mv4, exhibited an intermediate phenotype: reduced tube formation at 15 °C but more robust assembly than WT. These findings establish that decreasing coiled-coil stability systematically shifts the tube-forming temperature range toward lower temperatures.

Having established the stability-dependent temperature behaviour, we next tested whether these stability differences also manifest in the physical architecture of the resulting tubes. Given that our previous work[28] showed that PuuE tubes inherently exhibit a broad distribution of diameters, we sought to determine whether rational tuning of linker stability could shift this distribution in a predictable manner. To address this question, we quantified tube architectures across WT, Mv3, and Mv4. At 35 °C, the three variants again formed a clear stability-dependent series: PuuE-M(WT) produced the thinnest tubes, PuuE-Mv3 yielded intermediate diameters, and PuuE-Mv4 generated the thickest structures (**Fig. 3b, Supplementary Fig. 5**). Quantitative analysis clearly demonstrated that lower coiled-coil stability correlates with larger tube diameters, with Mv4 forming the thickest tubes and WT forming the thinnest (**Fig. 3c**). This systematic and reproducible diameter shift indicates that the naturally occurring morphological diversity of PuuE tubes can be deliberately biased through rational tuning of linker stability. Together, these observations support the idea that coiled-coil stability serves as a tunable structural parameter governing tube architecture.

Formation process and structural features of multi-tube architectures

236 Strikingly, tubes formed by PuuE-Mv4 at 35 °C were not only larger in diameter (**Fig. 4a**) but also displayed
237 multilayered architectures, including clearly identifiable tube-in-tube structures (**Fig. 4b, Supplementary**
238 **Fig. 6a**). Cryo-electron tomography (Cryo-ET) revealed tube-in-tube assemblies concentrically arranged in
239 up to four layers (**Supplementary Fig. 7a–d**), across multiple fields of view, indicating that nested
240 organisation is a recurrent structural feature rather than a rare event. In regions of thin ice, we frequently
241 observed distorted and incomplete multilayered states, including tubes that appeared markedly flattened,
242 consistent with deformation imposed by local ice-thickness constraints. We also observed tube-in-tube
243 assemblies in which the outer layer partially covered the inner tube or was locally discontinuous, leaving
244 segments of the inner tube exposed (**Supplementary Fig. 7e**). Together, these thin-ice-associated
245 deformations and outer-layer discontinuities support the interpretation that the higher-order assemblies are
246 flexible yet mechanically labile.
247
248 Such nested morphologies were not observed for PuuE-M(WT) or PuuE-Mv3 under the same conditions.
249 Importantly, multilayered architectures were observed exclusively for PuuE-Mv4; neither PuuE-M(WT)
250 nor the intermediate-stability variant PuuE-Mv3 displayed any evidence of tube-in-tube formation. To
251 examine how these higher-order architectures arise, we performed time-resolved nsTEM imaging of PuuE-
252 Mv4/PuuE-p mixtures incubated at 35 °C and analysed the evolution of tube morphologies over the course
253 of assembly (**Fig. 4 and Supplementary Fig. 6a**).
254
255 At early time points (0–30 min), only thin, single-walled tubes were detected, typically spanning several
256 hundred nanometres in length. After 1–2 h, thicker tubes became increasingly dominant, showing that tube
257 elongation and thickening continue well after initial nucleation. Importantly, multilayered or tube-in-tube
258 structures were not apparent during these stages, consistent with wall thickening occurring prior to the
259 emergence of higher-order organisation. By approximately 4 h, however, distinct tube-in-tube architectures
260 began to appear, in which a secondary tubular layer was observed either partially or fully nested within a
261 pre-existing primary tube. These multilayered structures remained stable from 4 h to 24 h, indicating that
262 once formed, the tube-in-tube architecture represents a stable and mature structural state rather than a
263 transient intermediate.
264
265 In addition to these multilayered states, nsTEM also revealed regions where adjacent tubes meet at
266 incomplete or misaligned junctions, as well as displaced wall segments (**Supplementary Fig. 6b**). These
267 structural irregularities were particularly apparent in PuuE-Mv4 and were occasionally observed during
268 early stages of tube growth. Although their functional significance cannot be determined from these

observations alone, the presence of such local instabilities indicates that the assembling tubes can temporarily adopt imperfect configurations during the growth.

This sequential progression—from thin tubes to thickened tubes, and ultimately to multilayered architectures—shows that only Mv4 accesses hierarchical tube morphologies under these conditions, whereas WT and Mv3 remain confined to single-walled architectures. Together, these observations indicate that tuning coiled-coil stability not only shifts the temperature window and diameter of tube formation, but also governs access to higher-order, hierarchical tubular states, including the emergence and stabilisation of multi-walled tube architectures.

Discussion

In this study, we demonstrated that deliberate tuning of coiled-coil stability—guided by deep-learning–based predictions from ThermoMPNN—provides a powerful means of controlling the assembly behaviour and final morphology of two-component protein tubes (**Fig. 1**). Although ThermoMPNN was developed to predict mutation-induced changes in protein thermal stability—most commonly to guide the identification of stabilising mutations[29,38-41]—our study employs it in an inverse manner. By systematically selecting destabilising mutations, we repurposed the model to modulate the energetics of the heterodimeric linker interaction, highlighting both the versatility of the tool and the modular advantage of our assembly design. Furthermore, although ThermoMPNN does not inherently support complex inference, we achieved pseudo-complex prediction by focusing solely on the coiled-coiled linker. This exemplifies the modularity built into our system, in which the scaffold and linker functions are fully separable.

By engineering a systematic, AI-assisted stability gradient within the M3L2/p66α heterodimeric linker, we showed that single-amino-acid substitutions can systematically shift the temperature window for tube formation and modulate tube diameter in a predictable manner (**Fig. 3b, c**). Critically, further destabilization enables access to hierarchical assembly states that are not observed for more stable variants under the same conditions, including multilayered tube-in-tube architectures (**Fig. 4b; Supplementary Fig. 7**). Time-resolved imaging further revealed that these hierarchical states emerge through a stepwise morphological transition—from thin tubes to wall-thickened intermediates, and ultimately to nested architectures—reflecting the increased dynamic rearrangements near the temperature range where the linker undergoes partial destabilization. Together, these findings demonstrate that local interaction energetics at a single heterodimeric interface can directly govern the macroscopic morphology of multi-component protein assemblies.

303 The results presented in this study reveal a clear and systematic relationship between the stability of the
304 M3L2/p66α heterodimeric linker and the morphology of the resulting two-component protein tubes (**Fig.**
305 **3, 4, and Table 1**). Across the engineered stability gradient—ranging from the most stable PuuE-M(WT),
306 through the intermediate variant Mv3, to the least stable Mv4—tube formation behaviour, temperature
307 sensitivity, tube diameter, and access to higher-order architectures all varied in a coherent and predictable
308 manner. This continuum of behaviours underscores the central role of local interaction energy in shaping
309 global assembly outcomes.
310
311 For PuuE-M(WT), the high stability of the coiled-coil interaction limits dynamic rearrangements even near
312 its T_m, resulting in a relatively narrow temperature window for tube formation and the production of thin,
313 single-walled tubes. In Mv3, moderate destabilisation weakens the interaction sufficiently to permit partial
314 tube formation at lower temperatures and to yield tubes of intermediate diameter, yet not enough to trigger
315 higher-order architectural transitions. In contrast, Mv4, the least stable linker, experiences substantial
316 transient weakening of the coiled-coil near its T_m, greatly increasing the frequency of dynamic linker
317 rearrangements. This enhanced dynamism enables growth processes not accessible in the more stable
318 variants—including progressive wall thickening and, ultimately, the formation of multilayered tube-in-tube
319 structures.
320
321 These differences in assembly behaviour are consistent with the intrinsic structural properties of the
322 engineered M3L2 variants. AF3 modelling indicated that, although both Mv3 and Mv4 introduce glycine
323 substitutions, their structural contexts differ in ways that directly impact coiled-coil stability (**Fig. 2e, f**).
324 Glycine is known to have one of the lowest intrinsic helix propensities among the canonical amino acids,
325 whereas alanine and arginine are comparatively helix-favouring, particularly in alanine-based model
326 helices[42]. In Mv3, the A14G substitution is positioned in a semi-exposed region where replacing alanine
327 with glycine is expected to modestly weaken local helical stability but not substantially disrupt the packing
328 interface, consistent with its intermediate phenotype. In contrast, the R16G mutation in Mv4 lies close to
329 interfacial packing and ionic contacts that stabilise the antiparallel heterodimer; replacing a bulky, helix-
330 compatible arginine side chain with glycine both creates a packing void and introduces a strong helix-
331 breaking residue at a structurally sensitive position. Positional studies in alanine-based helices have shown
332 that substitutions closer to the C-terminal region can exert disproportionately large effects on helicity
333 compared with substitutions nearer the N-terminus, consistent with enhanced sensitivity of C-terminal sites
334 to local perturbation[43]. These considerations provide a mechanistic rationale for why Mv3 remains confined
335 to single-walled tubes, whereas Mv4 accesses thickened and multilayered tube architectures through
336 enhanced dynamic rearrangements enabled by reduced coiled-coil stability. Our results establish that the

energetics of a single heterodimeric interaction can directly govern the macroscopic morphology of a multi-component protein assembly.

The structural intermediates accompanying this transition provide further mechanistic insight. nsTEM imaging revealed that PuuE-Mv4 frequently exhibits incomplete or misaligned junctions, as well as displaced wall segments (**Supplementary Fig. 6b**). Although similar structural irregularities may also arise in PuuE-M(WT) and Mv3, their consequences differ markedly among the variants. In Mv4, reduced coiled-coil stability creates a dynamic regime in which transient structural fluctuations arise more readily and, crucially, can be amplified into productive growth events. This heightened architectural potential enables Mv4 to convert local instabilities into initiation sites for secondary nucleation or lateral association, processes that are not observed for the more stable WT or intermediate-stability Mv3 linkers. These locally unstable configurations are therefore consistent with a model in which transient partial dissociation of the linker below its stability threshold enables the emergence of nested architectures by permitting reorganization and re-engagement of the assembling interfaces. Moreover, the experimentally observed temporal sequence—from thin tubes, through wall-thickened intermediates, and ultimately to mature tube-in-tube assemblies—aligns with this stability-dependent dynamic-rearrangement model. Importantly, this sequential progression indicates a path-dependent assembly process in which access to hierarchical tube architectures is kinetically gated, rather than arising from simultaneous multilayer formation. Together, these findings demonstrate that the capacity to access hierarchical morphologies is not determined solely by the presence of structural defects but by the linker's ability to exploit such transient irregularities. Local tuning of coiled-coil stability thus emerges as a minimal yet powerful lever for reshaping higher-order architecture, influencing assembly efficiency, temperature responsiveness, and access to complex hierarchical states.

The multilayered tube-in-tube architectures observed in PuuE-Mv4 resonate with the broader principle that many natural protein assemblies—such as clathrin cages[5,6], actin networks[2], and microtubules with variable protofilament numbers[13,44,45]—can access multiple geometric states through flexible and dynamic interaction modules. Although these biological systems operate within far more complex regulatory environments, our artificial scaffold captures an important aspect of this behaviour in a minimal and fully defined form. The appearance of local junctional irregularities and their subsequent amplification into higher-order architectures mirrors the way natural assemblies use transient structural fluctuations to diversify morphology. Thus, by tuning the stability of a single heterodimeric linker, we reveal a generalisable route for introducing natural-like architectural plasticity into designed protein assemblies,

370 providing a simple framework for exploring how dynamic interactions can give rise to hierarchical
371 structural diversity.
372
373 Although demonstrated here using the M3L2/p66α heterodimer and the tetrameric PuuE scaffold, these
374 results suggest that tuning the stability of a single interaction interface provides a general strategy for
375 controlling access to hierarchical assembly states in designed protein systems. Many naturally occurring
376 and engineered coiled-coils share modular architectures with well-defined positional roles of residues,
377 allowing their interaction energetics to be systematically tuned by minimal sequence modifications.
378 Likewise, the concept is not restricted to tubular assemblies: sheets, cages, or lattices that rely on linker-
379 mediated connectivity may also exhibit tunable morphology when the stability of the connecting element
380 is rationally modulated. Beyond expanding the design space for protein-based materials, stability-tuned
381 linkers may support the construction of assemblies that respond to external or physicochemical stimuli such
382 as temperature or ionic strength, suggesting applications in responsive biomaterials, encapsulation systems,
383 or programmable nanoscale scaffolds. Taken together, these observations indicate that stability modulation
384 of heterodimeric linkers can serve as a general handle for steering assembly outcomes, providing a
385 foundation for designing increasingly complex and functional protein architectures.
386
387 Having shown that linker stability can systematically influence tube morphology, we see several
388 opportunities for extending and refining this design framework. In this context, extending stability tuning
389 to orthogonal linkers and alternative protein backbones will be important for establishing the generality of
390 the approach. In addition, quantitative kinetic analyses may help reveal how the frequency and lifetime of
391 dynamic linker rearrangements depend on interaction energetics. More broadly, integrating stability tuning
392 with orthogonal design strategies—such as pH-responsive, ligand-gated, or redox-responsive linkers—may
393 enable the construction of fully programmable, multi-responsive assemblies with increasingly sophisticated
394 morphological and functional behaviours. Ultimately, this framework provides a starting point for creating
395 protein-based materials whose architectures and dynamics can be rationally guided through fine control of
396 local interaction stability.
397
398 **Methods**
399 **Computational engineering of the M3L2/p66α coiled-coil interaction**
400 The structure of M3L2-Gly_{50}-p66α was predicted using AlphaFold 2.3 (DeepMind)[32]. The most reliable
401 model (ranked_0 model) was used as the input for ThermoMPNN[29] to infer $\Delta\Delta G_{Pred}$ values for all possible
402 single-mutations. The resulting $\Delta\Delta G_{Pred}$ scores were examined, and for the previously reported coiled-coil
403 key residues in M3L2, the most destabilising mutation ($\Delta\Delta G_{Pred} > 0$) was selected. The overall

404 computational workflow is summarized in **Fig. 1**, and the selected mutations are listed in **Table 1** and
405 **Supplementary Table 1**. Amino acid sequences for all constructs used in this study are provided in
406 **Supplementary Table 2**.
407
408 **Plasmids and cloning**
409 The plasmids encoding N-terminal 6×His-TEVcs-tagged PuuE-M(WT) and PuuE-p were previously
410 constructed. The plasmids encoding N-terminal 6×His-TEVcs-tagged M3L2(WT) and p66α were generated
411 from the PuuE-M(WT) and PuuE-p plasmids, respectively, by removal of the PuuE coding region. The
412 plasmid encoding N-terminal 8×His-TEVcs-tagged M3L2(WT) was generated from the 6×His-TEVcs-
413 M3L2(WT) plasmid by introducing two additional His codons. The plasmids encoding N-terminal 8×His-
414 TEVcs-tagged Mv series (Mvs) and 6×His-TEVcs-tagged PuuE-Mv series (PuuE-Mvs) were generated
415 from the 8×His-TEVcs-M3L2(WT) and PuuE-M(WT) plasmids, respectively, by site-directed substitution
416 of the corresponding codons. All primers used in this study were purchased from Eurofins Genomics, and
417 all primer sequences are shown in **Supplementary Data 1**. Mutagenesis was performed using the KOD -
418 Plus- Mutagenesis Kit (TOYOBO) according to the manufacturer's instructions. The 6×His-TEVcs-
419 M3L2(WT), 8×His-TEVcs-M3L2(WT), Mvs, and p66α plasmids were amplified in *E. coli* strain BL21
420 (DE3) derived ECOS SONIC competent cells (NIPPON GENE) and extracted using the NucleoSpin
421 Plasmid EasyPure (MACHEREY-NAGEL) according to the manufacturer's protocol. The PuuE-Mvs
422 plasmids were amplified in *E. coli* strain DH5α (NIPPON GENE) and purified using the same procedure.
423 All construct sequences were verified by Eurofins Genomics. Amino acid sequences for all constructs used
424 in this study are provided in **Supplementary Table 2**.
425
426 **Protein expression and purification**
427 The recombinant proteins of N-terminal 6× or 8×His-TEVcs-tagged M3L2(WT), Mvs, and p66α were
428 expressed using *E. coli* strain BL21 (DE3) derived ECOS SONIC competent cells as follows. Glycerol
429 stocks of transformed cells were used to inoculate 5 mL of liquid LB broth supplemented with 100 μg/mL
430 ampicillin (Amp) and grown overnight at 37 °C and 200 rpm. Overnight cultures were diluted into 1 L of
431 LB-Amp broth and grown at 37 °C and 200 rpm until reaching an optical density at 600 nm of 0.4–0.6.
432 Protein expression was induced by adding 0.1 mM isopropyl-β-D-thiogalactopyranoside, and the cultures
433 were grown at 16 °C for 18–20 h. Cells were harvested by centrifugation at 15,317 × *g* for 5 min at 4 °C
434 and stored at –80 °C.
435
436 The recombinant proteins of PuuE-M(WT), PuuE-Mvs, and PuuE-p were expressed using *E. coli* strain
437 BL21 (DE3) (NIPPON GENE) co-transformed with a pGro7 chaperone plasmid (Takara Bio). After

438 transformation, colonies grown overnight on LB agar plates supplemented with Amp and 20 μg/mL
439 chloramphenicol (Crm) at 37 °C were used to inoculate 5 mL of liquid LB-Amp-Crm broth and cultured
440 overnight at 37 °C and 200 rpm. Overnight cultures were diluted into 1 L of liquid LB-Amp-Crm broth
441 supplemented with 0.5 mg/mL L-arabinose and grown at 37 °C and 200 rpm until reaching an optical
442 density at 600 nm of 0.4–0.6. Protein induction and cells harvest was performed as described above.
443
444 All recombinant proteins were purified as follows. Cell pellets were thawed at 37 °C, resuspended in 60
445 mL of ice-cold purification buffer (20 mM Tris-HCl, pH 8.0, containing 300 mM NaCl), and lysed by
446 sonication (9 min, 1:2 on/off cycles, 70% amplitude; SFX250, Branson) on ice. Cell debris was removed
447 by centrifugation at 15,317 × *g* for 30 min at 4 °C. The supernatants were passed through a 0.45-μm pore
448 size membrane filter (Merck), loaded onto a HisTrap FF crude column (Cytiva) pre-equilibrated with the
449 purification buffer, and washed with 5 column volumes of 2% elution buffer (20 mM Tris-HCl, pH 8.0,
450 containing 300 mM NaCl and 1 M imidazole; 2% means 20 mM imidazole). Target proteins were eluted
451 with 10 column volumes of elution buffer with a linear gradient of 2–40% (i.e., 20–400 mM imidazole).
452 Fractions containing the target proteins as verified by UV absorbance and SDS-PAGE were dialysed twice
453 against a 50-fold volume of experimental buffer (50 mM Tris-HCl, pH 8.0, containing 100 mM NaCl and
454 0.5 mM EDTA) at 4 °C. Purified proteins were concentrated by Amicon Ultra centrifugal filter unit (Merck)
455 with an appropriate molecular weight cutoff, followed by filtration through a 0.45 μm pore size membrane
456 filter (Merck). Protein concentrations were determined by measuring absorbance at 280 nm using a
457 NanoDrop OneC spectrophotometer (Thermo Scientific). The molar extinction coefficients at 280 nm for
458 the proteins were calculated based on amino acid composition[46]. The concentrated proteins were flash-
459 frozen in liquid nitrogen and stored at –80 °C until use.
460
461 **Circular dichroism (CD) spectrum measurements**
462 All proteins were thawed immediately before CD measurements and kept on ice. Each sample was prepared
463 in a 1.5-mL microtube using experimental buffer to adjust the final protein concentration to 5.0 μM for
464 single-component samples or 2.5 + 2.5 μM for binary complexes, in a total volume of 200 μL at 25 ± 1 °C.
465 Far-UV CD spectra were recorded at a wavelength of 195 to 250 nm using a J-1100 spectropolarimeter
466 (JASCO) equipped with a 1-mm-path-length quartz cuvette, at the temperatures indicated in the manuscript.
467
468 Thermal denaturation measurements were performed over a temperatures range of 0 to 60 °C, with a heating
469 rate of 1 °C/min, while monitoring ellipticity at 222 nm. All spectra data were collected using Spectra
470 Manager version 2.5 (JASCO) and expressed as mean residue ellipticity. The T_m value of each sample was

471 determined from the thermal denaturation curve by sigmoid fitting using Igor Pro 9 version 9.0.5.1
472 (WaveMetrics).
473
474 **Tube formation**
475 All proteins were thawed immediately before tube formation experiments and kept on ice. Each sample was
476 prepared in a 1.5-mL microtube using experimental buffer to adjust the concentration as indicated in the
477 figure legends, with a final volume of 100 μL at 25 ± 1 °C. Sample incubation was performed using a
478 ThermoMixer C (Eppendorf) or a MATRIX Orbital Delta Plus (IKA) with shaking at 300 rpm, at the
479 temperatures described in the manuscript.
480
481 **Negative-stain transmission electron microscopy (nsTEM)**
482 A naked G600TT copper grid (Nisshin EM) was carbon-coated using a VE-2030 (VACUUM DEVICE).
483 The grid was glow-discharged using a PIB-10 (VACUUM DEVICE). Then, a 5-μL aliquot of the sample
484 solution was placed on the grid for 1 min, and the remaining solution was removed with filter paper (No. 2,
485 ADVANTEC) followed by rinsing thrice with a 5-μL aliquot of Milli-Q water. After blotting off the water
486 with filter paper, the sample was stained briefly with a 3-μL aliquot of 2% (w/v) uranyl acetate solution
487 three times. The remaining solution was removed with filter paper and the grid was dried on the benchtop.
488 TEM observation was performed using a transmission electron microscope HT-7700 (Hitachi) with an
489 acceleration voltage of 80 kV. The images were recorded using HT-7700 control software version 02.22
490 (Hitachi).
491
492 **Cryo-electron tomography (Cryo-ET)**
493 A 2.7-μl aliquot of specimen solution was applied onto glow-discharged Quantifoil R1.2/1.3 Gold 200
494 mesh grids (Quantifoil Micro Tools GmbH). After blotting excess solution from the grids with filter paper,
495 specimens were rapidly frozen in liquid ethane on a Vitrobot Mark IV (Thermo Fisher Scientific). Cryo-
496 ET datasets were collected using a Glacios cryo-TEM (Thermo Fisher Scientific) operated at an
497 acceleration voltage of 200 kV, equipped with a Falcon4 direct electron detector at the Institute for Life
498 and Medical Sciences, Kyoto University. Tilt-series were collected with a dose-symmetric tilt scheme[47]
499 using TEM Tomography 5 software (Thermo Fisher Scientific). The tilt span of ±60° was used in 3°
500 increments, starting at 0°. All tilt-series were collected in nanoprobe mode with a defocus of -4.0 μm and
501 TIFF compression enabled. Data were acquired at a dose rate of 10.6 e^{-}/pixel/s, a pixel size of 1.55 Å, and
502 a total exposure of 144 $e^{-}/Å^{2}$ per tilt series. Eucentric height estimation was performed once for each tilt
503 angle using stage-tilt method in TEM Tomography 5 software. Regions of interest were added manually,
504 and positions were saved. Tracking and focusing were performed before and after each tilt step. All data

were processed using RELION-5 tomography pipeline[48]. TIFF movie frames were motion corrected using RELION's own implementation and gain normalisation using a gain reference image generated by the "relion_estimate_gain" command in RELION-5. Tilt-series alignment was performed using AreTomo2[49], which simultaneously estimates the contrast transfer function (CTF) for each tilt image during alignment. The aligned tilt series were subsequently used to reconstruct tomograms. All tomographic reconstructions were binned to yield a final pixel size of 12.4 Å, and were visualized using IMOD software package[50].

Tube diameter analysis

For each sample incubated at 35 °C, more than 200 clearly discernible tubes were picked up manually on 10k-magnification nsTEM images. Tube segments in which tubes overlapped were excluded from analysis. Tube diameters were measured using ImageJ (Fiji) version 1.53[51]. For quantitative comparison, a representative subset of 150 tubes was selected from the measurable population using the same inclusion criteria across all samples, focusing on the larger-diameter species that predominated under the tube-forming conditions. Diameter distributions and plots were generated using Igor Pro 9.

Molecular modelling

The structure of M3L2-Gly_{50}-p66α, PuuE-M(WT), and PuuE-p was predicted by AlphaFold 2.3 (DeepMind)[32,52]. All other predicted protein structures were generated using AlphaFold 3 (DeepMind)[33]. Cartoon representations of protein models were drawn using PyMOL version 2.5 (Schrödinger)[53] and UCSF ChimeraX version 1.9 (UCSF RBVI and NIH)[54].

Statistics and Reproducibility

For the analysis of tube diameter, a two-sided Welch's *t* test was performed to test the null hypothesis, and the exact *p* values are provided in the figure legend. Each of the tube formation experiment was repeated using at least two biological replicates, and consistent results were confirmed by nsTEM.

References

1 Korn, E. D., Carlier, M. F. & Pantaloni, D. Actin polymerization and ATP hydrolysis. *Science* **238**, 638-644 (1987).

2 Pollard, T. D. & Cooper, J. A. Actin, a central player in cell shape and movement. *Science* **326**, 1208-1212 (2009).

3 Block, J., Schroeder, V., Pawelzyk, P., Willenbacher, N. & Koster, S. Physical properties of cytoplasmic intermediate filaments. *Biochim Biophys Acta* **1853**, 3053-3064 (2015).

4 Gudimchuk, N. B. & McIntosh, J. R. Regulation of microtubule dynamics, mechanics and function through the growing tip. *Nat Rev Mol Cell Biol* **22**, 777-795 (2021).

5 Fotin, A. et al. Molecular model for a complete clathrin lattice from electron cryomicroscopy. *Nature* **432**, 573-579 (2004).

6 Morris, K. L. et al. Cryo-EM of multiple cage architectures reveals a universal mode of clathrin self-assembly. *Nat Struct Mol Biol* **26**, 890-898 (2019).
7 Perlmutter, J. D. & Hagan, M. F. Mechanisms of virus assembly. *Annu Rev Phys Chem* **66**, 217-239 (2015).
8 Sevvana, M., Klose, T. & Rossmann, M. G. Principles of Virus Structure. *Encyclopedia of Virology*, 257-277 (2021).
9 Kaksonen, M. & Roux, A. Mechanisms of clathrin-mediated endocytosis. *Nat Rev Mol Cell Biol* **19**, 313-326 (2018).
10 Sugita, Y., Matsunami, H., Kawaoka, Y., Noda, T. & Wolf, M. Cryo-EM structure of the Ebola virus nucleoprotein-RNA complex at 3.6 A resolution. *Nature* **563**, 137-140 (2018).
11 Zhou, R. Q. et al. Structure and assembly of the alpha-carboxysome in the marine cyanobacterium Prochlorococcus. *Nat Plants* **10**, 661-672 (2024).
12 Hvorecny, K. L., Sladewski, T. E., De La Cruz, E. M., Kollman, J. M. & Heaslip, A. T. Toxoplasma gondii actin filaments are tuned for rapid disassembly and turnover. *Nat Commun* **15**, 1840 (2024).
13 Chalfie, M. & Thomson, J. N. Structural and functional diversity in the neuronal microtubules of Caenorhabditis elegans. *J Cell Biol* **93**, 15-23 (1982).
14 Fukushige, T. et al. MEC-12, an alpha-tubulin required for touch sensitivity in C. elegans. *J Cell Sci* **112 (Pt 3)**, 395-403 (1999).
15 Bai, Y., Luo, Q. & Liu, J. Protein self-assembly via supramolecular strategies. *Chem Soc Rev* **45**, 2756-2767 (2016).
16 Huang, P. S., Boyken, S. E. & Baker, D. The coming of age of de novo protein design. *Nature* **537**, 320-327 (2016).
17 Gainza-Cirauqui, P. & Correia, B. E. Computational protein design-the next generation tool to expand synthetic biology applications. *Curr Opin Biotechnol* **52**, 145-152 (2018).
18 Kuhlman, B. & Bradley, P. Advances in protein structure prediction and design. *Nat Rev Mol Cell Biol* **20**, 681-697 (2019).
19 Zhu, J. et al. Protein Assembly by Design. *Chem Rev* **121**, 13701-13796 (2021).
20 Kortemme, T. De novo protein design-From new structures to programmable functions. *Cell* **187**, 526-544 (2024).
21 King, N. P. et al. Accurate design of co-assembling multi-component protein nanomaterials. *Nature* **510**, 103-108 (2014).
22 Bale, J. B. et al. Accurate design of megadalton-scale two-component icosahedral protein complexes. *Science* **353**, 389-394 (2016).
23 Ben-Sasson, A. J. et al. Design of biologically active binary protein 2D materials. *Nature* **589**, 468-473 (2021).
24 Wang, S. et al. Bond-centric modular design of protein assemblies. *Nat Mater* **24**, 1644-1652 (2025).
25 Brodin, J. D. et al. Metal-directed, chemically tunable assembly of one-, two- and three-dimensional crystalline protein arrays. *Nat Chem* **4**, 375-382 (2012).
26 Huddy, T. F. et al. Blueprinting extendable nanomaterials with standardized protein blocks. *Nature* **627**, 898-904 (2024).
27 Koziej, L. et al. Dynamic Assembly of Pentamer-Based Protein Nanotubes. *ACS Nano* **19**, 8786-8798 (2025).
28 Noji, M., Sugita, Y., Yamazaki, Y., Miyazaki, M. & Suzuki, Y. Protein design of two-component tubular assemblies similar to cytoskeletons. *Nat Commun* **16**, 6738 (2025).
29 Dieckhaus, H., Brocidiacono, M., Randolph, N. Z. & Kuhlman, B. Transfer learning to leverage larger datasets for improved prediction of protein stability changes. *Proc Natl Acad Sci U S A* **121**, e2314853121 (2024).
30 Gnanapragasam, M. N. et al. p66Alpha-MBD2 coiled-coil interaction and recruitment of Mi-2 are critical for globin gene silencing by the MBD2-NuRD complex. *Proc Natl Acad Sci U S A* **108**, 7487-7492 (2011).

31 Walavalkar, N. M., Gordon, N. & Williams, D. C., Jr. Unique features of the anti-parallel, heterodimeric coiled-coil interaction between methyl-cytosine binding domain 2 (MBD2) homologues and GATA zinc finger domain containing 2A (GATAD2A/p66alpha). *J Biol Chem* **288**, 3419-3427 (2013).

32 Jumper, J. et al. Highly accurate protein structure prediction with AlphaFold. *Nature* **596**, 583-589 (2021).

33 Abramson, J. et al. Accurate structure prediction of biomolecular interactions with AlphaFold 3. *Nature* **630**, 493-500 (2024).

34 Wee, J. & Wei, G. W. Evaluation of AlphaFold 3's Protein-Protein Complexes for Predicting Binding Free Energy Changes upon Mutation. *J Chem Inf Model* **64**, 6676-6683 (2024).

35 Lu, W., Zhang, J., Rao, J., Zhang, Z. & Zheng, S. AlphaFold3, a secret sauce for predicting mutational effects on protein-protein interactions. *bioRxiv* (2024).

36 Watanabe, K., Masuda, T., Ohashi, H., Mihara, H. & Suzuki, Y. Multiple proline substitutions cumulatively thermostabilize Bacillus cereus ATCC7064 oligo-1,6-glucosidase. Irrefragable proof supporting the proline rule. *Eur J Biochem* **226**, 277-283 (1994).

37 Watanabe, K. & Suzuki, Y. Protein thermostabilization by proline substitutions. *J Mol Catal B-Enzym* **4**, 167-180 (1998).

38 Peccati, F., Segovia, C. M., Núñez-Franco, R. & Jimenez-Oses, G. Computation of Protein Thermostability and Epistasis. *Wires Comput Mol Sci* **15** (2025).

39 Cui, X. C., Zheng, Y., Liu, Y., Yuchi, Z. & Yuan, Y. J. AI-driven de novo enzyme design: Strategies, applications, and future prospects. *Biotechnol Adv* **82**, 108603 (2025).

40 Sun, C. et al. Iterative recombinase technologies for efficient and precise genome engineering across kilobase to megabase scales. *Cell* **188**, 4693-4710 e4615 (2025).

41 Ou, W., Dan, J., Guo, X., Liu, Q. & Tan, L. An Integrative Strategy Enhancing Nanobody Thermostability via CDR Grafting, In Silico Mutagenesis Screening, and Multiplex Evaluation. *ACS Synth Biol* **14**, 2690-2702 (2025).

42 Chakrabartty, A., Kortemme, T. & Baldwin, R. L. Helix propensities of the amino acids measured in alanine-based peptides without helix-stabilizing side-chain interactions. *Protein Sci* **3**, 843-852 (1994).

43 Cheng, R. P. et al. Positional effects on helical Ala-based peptides. *Biochemistry* **49**, 9372-9384 (2010).

44 Chaaban, S. & Brouhard, G. J. A microtubule bestiary: structural diversity in tubulin polymers. *Mol Biol Cell* **28**, 2924-2931 (2017).

45 Ferreira, J. L. et al. Variable microtubule architecture in the malaria parasite. *Nat Commun* **14**, 1216 (2023).

46 Pace, C. N., Vajdos, F., Fee, L., Grimsley, G. & Gray, T. How to measure and predict the molar absorption coefficient of a protein. *Protein Sci* **4**, 2411-2423 (1995).

47 Hagen, W. J. H., Wan, W. & Briggs, J. A. G. Implementation of a cryo-electron tomography tilt-scheme optimized for high resolution subtomogram averaging. *J Struct Biol* **197**, 191-198 (2017).

48 Burt, A. et al. An image processing pipeline for electron cryo-tomography in RELION-5. *FEBS Open Bio* **14**, 1788-1804 (2024).

49 Zheng, S. et al. AreTomo: An integrated software package for automated marker-free, motion-corrected cryo-electron tomographic alignment and reconstruction. *J Struct Biol X* **6**, 100068 (2022).

50 Kremer, J. R., Mastronarde, D. N. & McIntosh, J. R. Computer visualization of three-dimensional image data using IMOD. *J Struct Biol* **116**, 71-76 (1996).

51 Schindelin, J. et al. Fiji: an open-source platform for biological-image analysis. *Nat Methods* **9**, 676-682 (2012).

52 Evans, R. et al. Protein complex prediction with AlphaFold-Multimer. *bioRxiv*, 2021.2010.2004.463034 (2022).

53 Schrodinger, LLC. *The PyMOL Molecular Graphics System, Version 2.5*.

54 Meng, E. C. et al. UCSF ChimeraX: Tools for structure building and analysis. *Protein Sci* **32**, e4792 (2023).

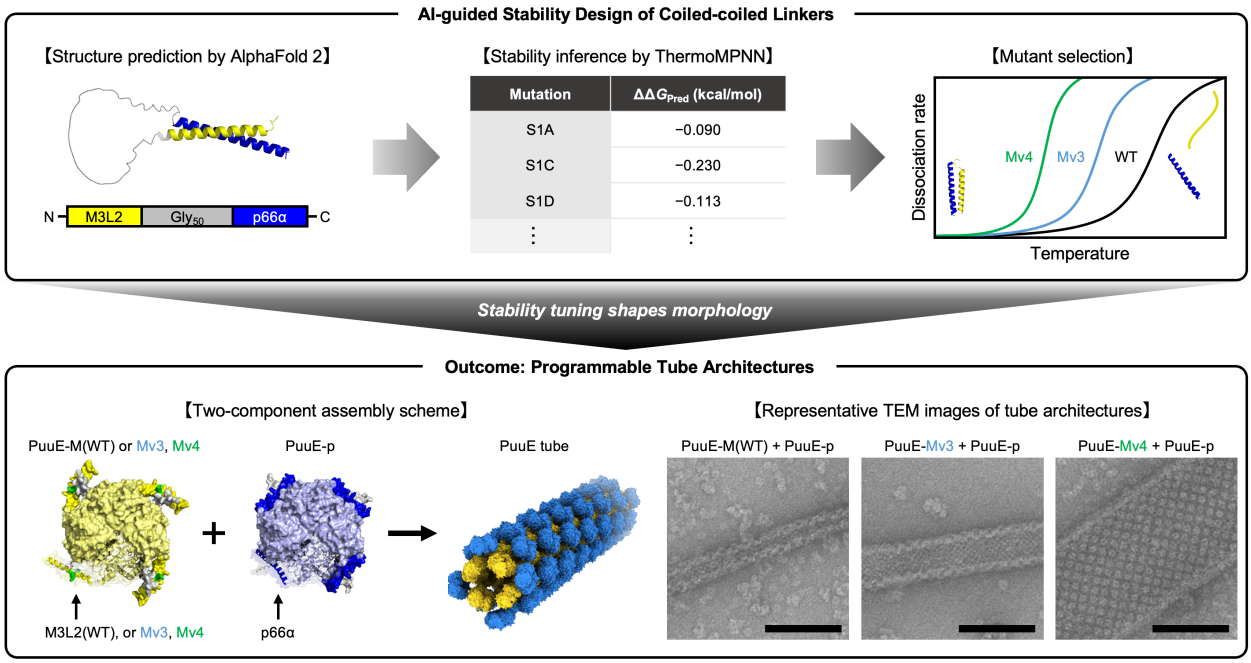

Fig. 1. AI-guided stability tuning of a heterodimeric coiled-coil linker enables programmable protein tube architectures. | Design workflow for generating stability-tunable M3L2/p66α coiled-coil variants using AF2 structural modelling, ThermoMPNN $\Delta\Delta G$ predictions, and selection of mutants spanning an engineered stability gradient (top). Assembly schematic and representative TEM images illustrating architecture-specific tube morphologies obtained with each variant (bottom). Stability-tuned M3L2 variants yield distinct tube architectures—thin (WT), intermediate (Mv3), and thick (Mv4)—upon assembly with PuuE-p. Scale bar, 100 nm.

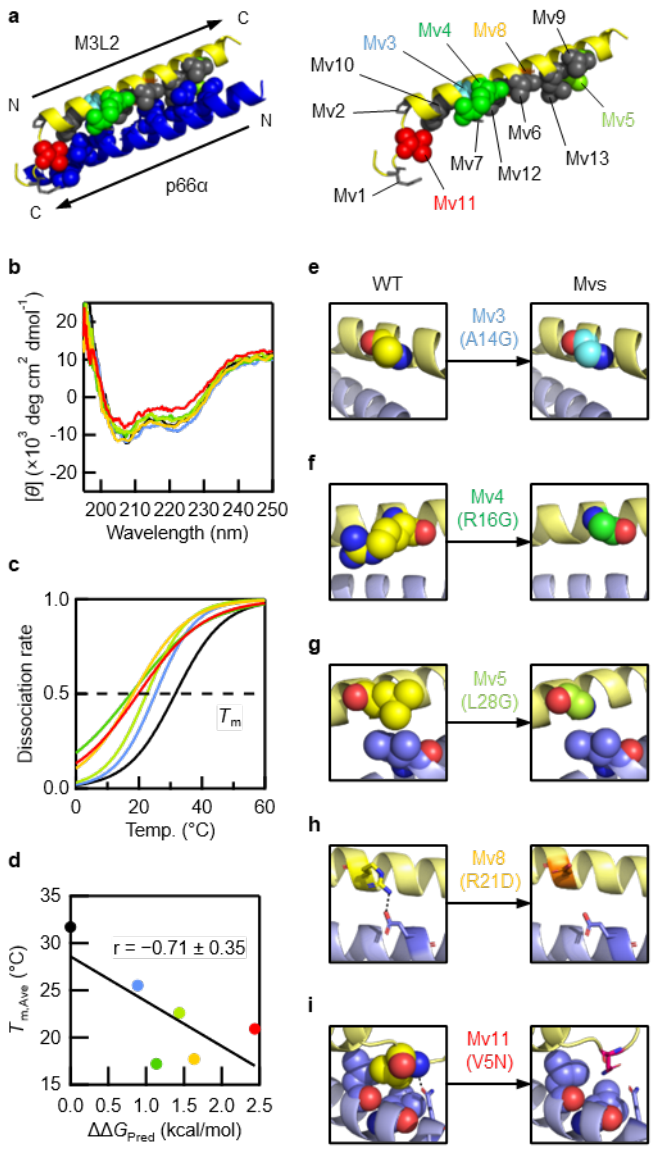

Fig. 2. Deep-learning-guided engineering generates a predictable and experimentally validated coiled-coil stability gradient. | a, Schematic representations of the M3L2/p66α heterodimeric coiled-coil predicted by AF3 (left) and the targeted mutation sites (right). **b,** CD spectra of WT and selected M3L2 mutants complexed with p66α indicating preserved coiled-coil secondary structure. **c,** Thermal denaturation profiles of WT and selected M3L2 mutants. **d,** Correlation between ThermoMPNN-predicted $\Delta\Delta G_{\mathrm{Pred}}$ values and the experimentally determined $T_{\mathrm{m,Ave}}$. **e–i,** AF3 structural models illustrating mutation-dependent local perturbations within the M3L2/p66α interface. Mutated residues are shown in space-filling (ball) representation to highlight steric volume and hydrophobic packing effects, whereas neighbouring residues involved in hydrogen-bonding or other directional interactions are shown in stick representation to visualise how each substitution alters the local interaction environment.

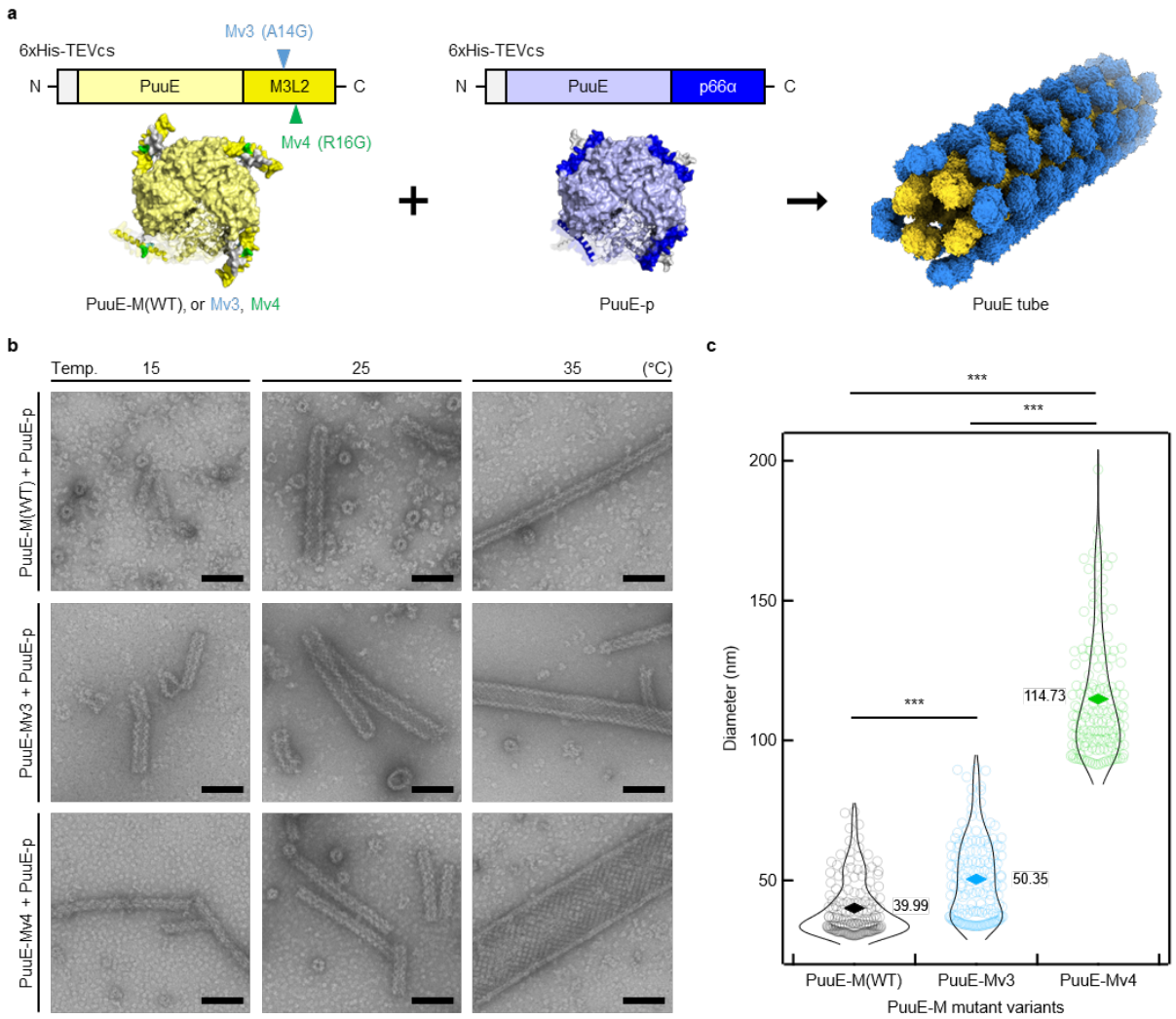

Fig. 3. M3L2/p66α coiled-coil stability dictates the temperature-dependent formation and morphology of two-component protein tubes. | a, Schematic representation of the two-component tube-forming system, showing PuuE-M(WT) or its stability-tuned variants (PuuE-Mv3, PuuE-Mv4) paired with PuuE-p via the C-terminal M3L2/p66α heterodimeric linker. **b,** Representative nsTEM images of tubes formed by PuuE-M(WT), PuuE-Mv3, and PuuE-Mv4 in complex with PuuE-p at 15, 25, and 35 °C. Additional representative TEM images across temperatures are provided in **Supplementary Fig. 5**. **c,** Quantified tube diameter distributions for PuuE-M(WT), PuuE-Mv3, and PuuE-Mv4 after 24 h of incubation at 35 °C. Mean values are shown with diamond-shaped markers. $^{***}p < 0.001$ (p-values; WT–Mv3 = 4.21×10^{-12}, Mv3–Mv4 = 8.87×10^{-88}, and WT–Mv4 = 2.11×10^{-97}, two-sided Welch's t test). Scale bar, 100 nm.

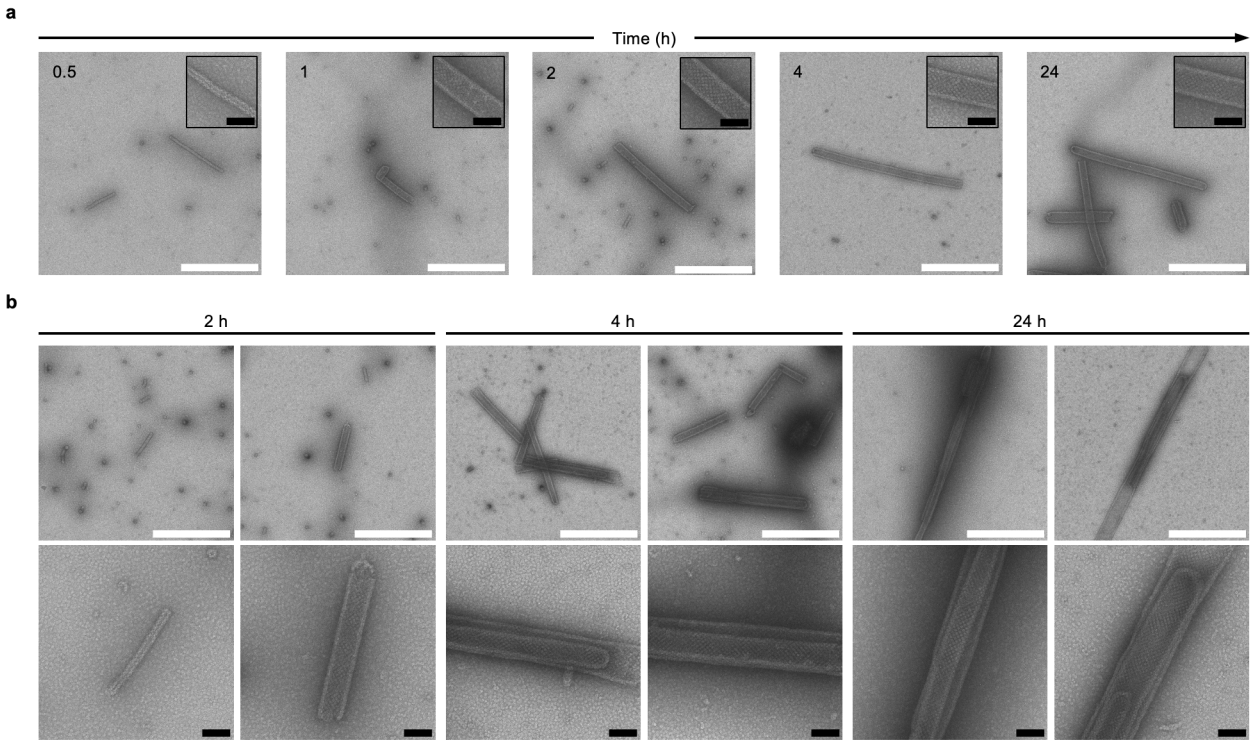

Fig. 4. Reduced coiled-coil stability enables a hierarchical tube-in-tube assembly pathway through transient structural intermediates. | a, Time-resolved nsTEM images of PuuE-Mv4 assembled with PuuE-p at 35 °C, illustrating the progressive elongation of tubes over time (0.5, 1, 2, 4, and 24 h). Insets show magnified views of representative tube segments at each time point. **b,** Representative nsTEM images comparing tubes lacking tube-in-tube features (2 h) with those in which tube-in-tube architectures begin to appear (4 h) and fully develop (24 h). Additional time points and further representative images are provided in **Supplementary Fig. 6**. Scale bars: white, 1 μm; black, 100 nm.

Name	Mutation	$\Delta\Delta G_{Pred}$ (kcal/mol)	$T_{m,Ave}$ (°C)
WT	None	None (= 0)	31.7
Mv3	A14G	0.888	25.5
Mv4	R16G	1.136	17.2
Mv5	L28G	1.443	22.6
Mv8	R21D	1.637	17.7
Mv11	V5N	2.439	20.9

Table 1. M3L2 wild-type and selected mutants. | Predicted stability changes for point mutations ($\Delta\Delta G_{Pred}$) derived from ThermoMPNN inference are shown for M3L2 wild-type (WT) and its selected mutants (Mvs). Averaged melting temperatures ($T_{m,Ave}$) determined from CD measurements are provided for coiled-coil complexes formed between p66α and each variant. Source data are provided as a Source Data file.

Acknowledgements

This work was supported by JSPS KAKENHI (grant nos. 19H02832, 19K22253, and 21H05116 to Yuta Suzuki (Y. Suzuki); 21H05117 to Y. Suzuki and Yukihiko Sugita (Y. Sugita); and 20K22628, 21J00530, and 22KJ1644 to M.N.), JST PRESTO (grant no. JPMJPR22A7 to Y. Suzuki.), Takeda Science Foundation to Y. Suzuki, Chubei Itoh Foundation to Y. Suzuki, and The Hakubi Center for Advanced Research to Y. Sugita, and Y. Suzuki.

Author contributions Statement

Y. Suzuki directed the project and led the conceptual framework. M.N. and Y. Suzuki conceived and designed the study. M.N. performed all experiments except cryo-EM and analysed the data with Y.Suzuki. providing interpretative guidance. T.F., Y. Sugita and M.N. performed cryo-EM data collection, and T.F. and Y. Sugita analysed the cryo-EM data. Y.Suzuki and M.N. wrote the manuscript with contributions from T.F. and Y. Sugita.

Supplementary Figures

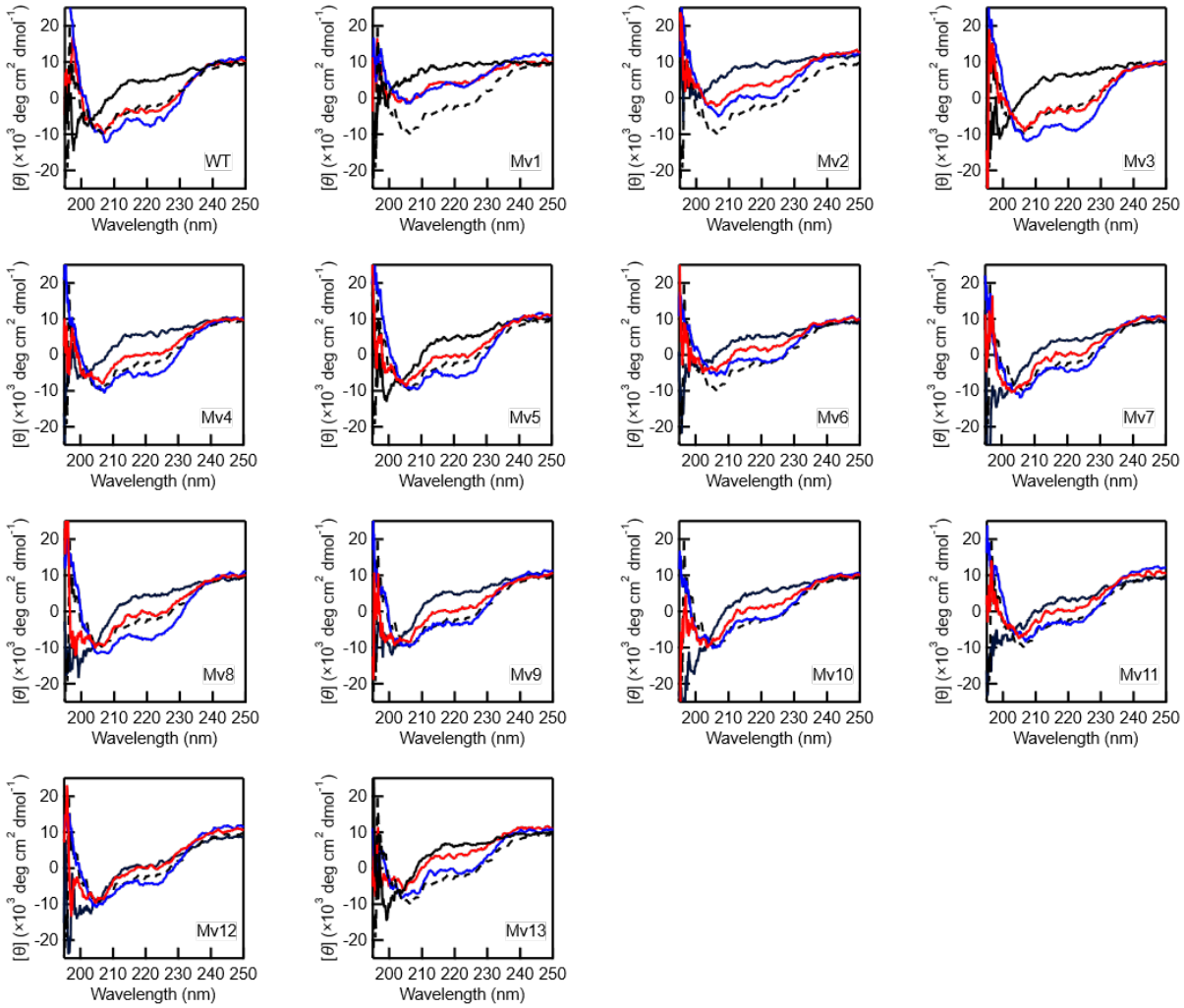

Supplementary Fig. 1. Coiled-coil formation of M3L2(WT) and Mvs. | CD spectra for isolated M3L2 variants (solid black lines) and p66α (dashed black lines) measured at 25 °C, as well as spectra for mixtures of each variant with p66α measured at 5 °C and 25 °C (blue and red lines, respectively). All spectra are labelled with the corresponding construct names. Source data are provided as a Source Data file.

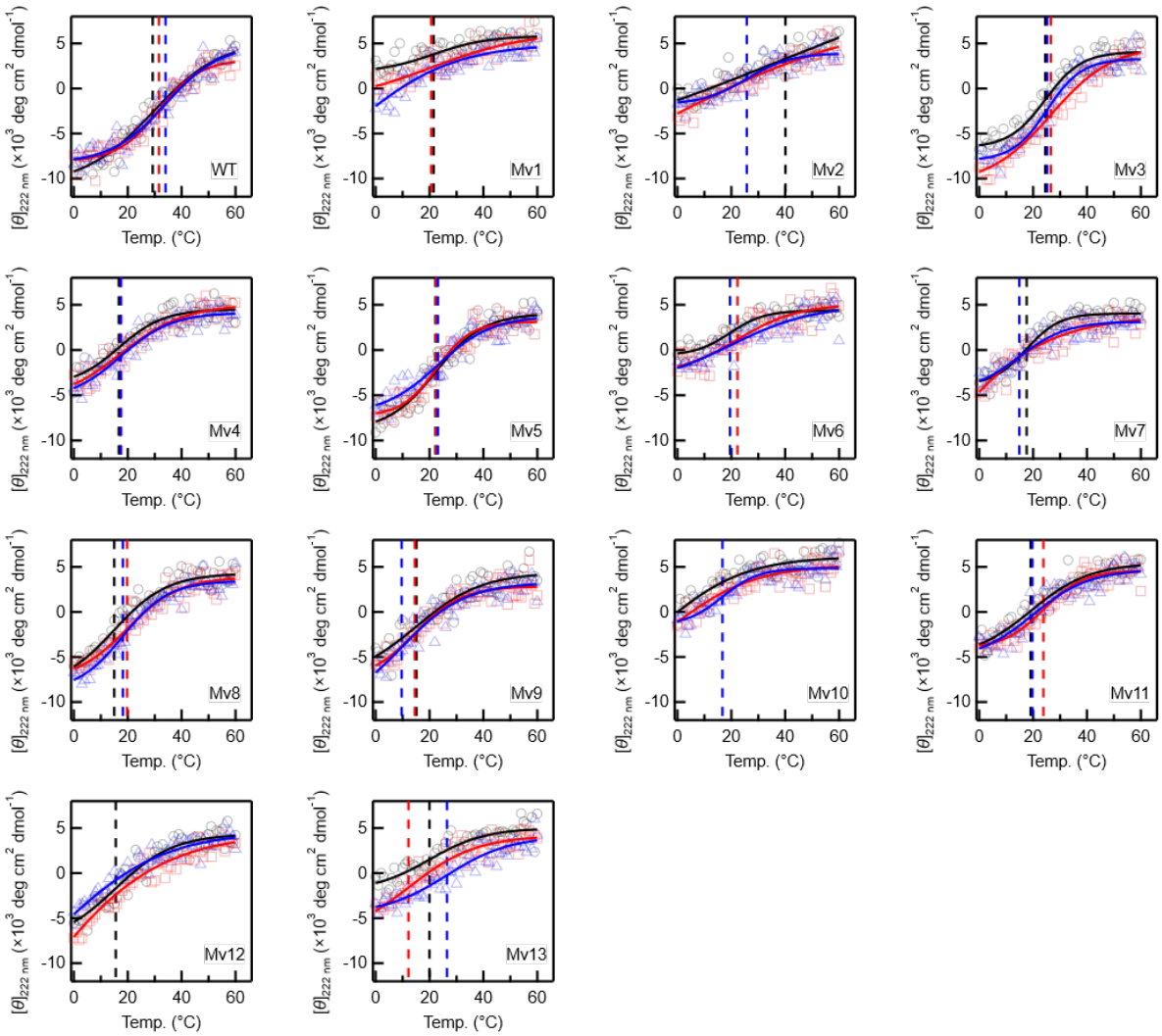

Supplementary Fig. 2. Thermal stability of M3L2(WT) and Mvs. | Thermal denaturation curves of mixtures of M3L2 variants with p66α recorded from 0 to 60 °C. For each variant, three independent experiments were performed; individual $\theta_{222\ \mathrm{nm}}$ values are plotted with different markers. Fitted curves (solid lines) and the extracted T_m values (dashed lines) are shown in matching colours for each dataset. Numerical T_m and the calculated $T_{m,Ave}$ values are summarised in **Supplementary Table 1**. Source data are provided as a Source Data file.

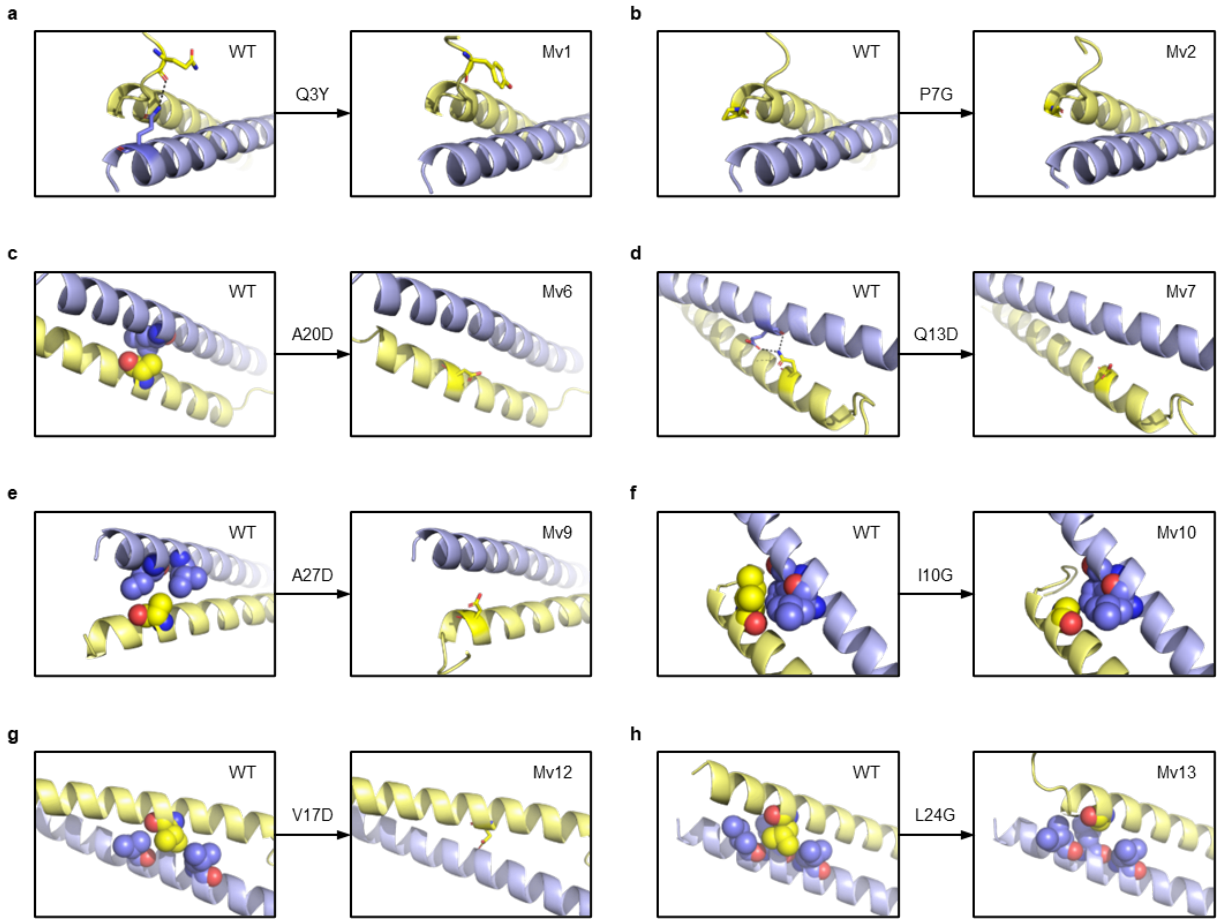

Supplementary Fig. 3. AF3 structural prediction of Mvs/p66α coiled-coil complexes. | a–h, the most reliable AF3-predicted models of WT (left) and each Mv variant (right) in complex with p66α, excluding the models shown in Fig. 2. For each model, the region surrounding the mutated residue is enlarged. Mutated residues and interacting partners are shown in ball (space-filling) or stick representations, with interchain hydrogen bonds indicated by dashed lines.

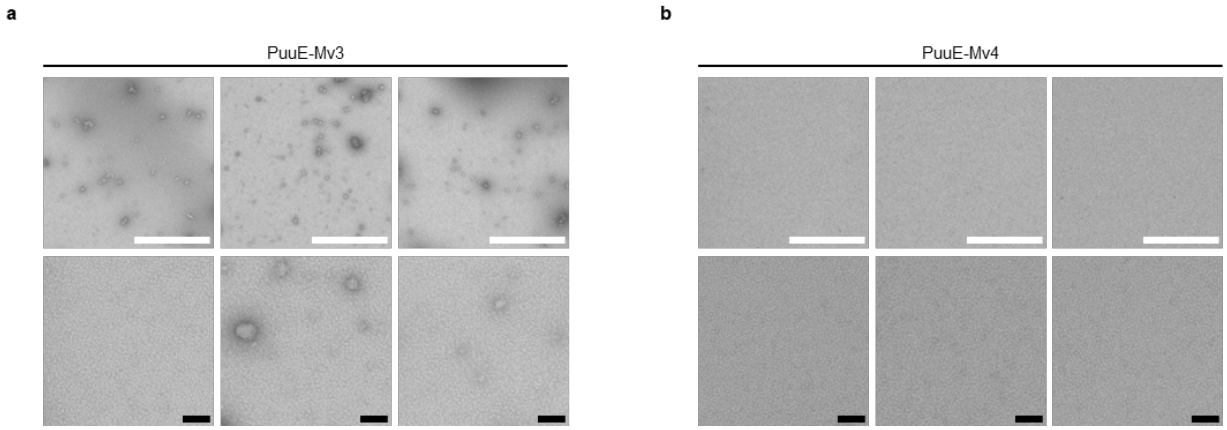

Supplementary Fig. 4. nsTEM images of PuuE-Mvs in the absence of PuuE-p. | a, b, Representative nsTEM images of PuuE-Mv3 (**a**) and PuuE-Mv4 (**b**). 12.5 μM PuuE-Mvs in experimental buffer was incubated at 25 °C for 24 h and imaged via nsTEM. Scale bars, 1 μm (white), 100 nm (black).

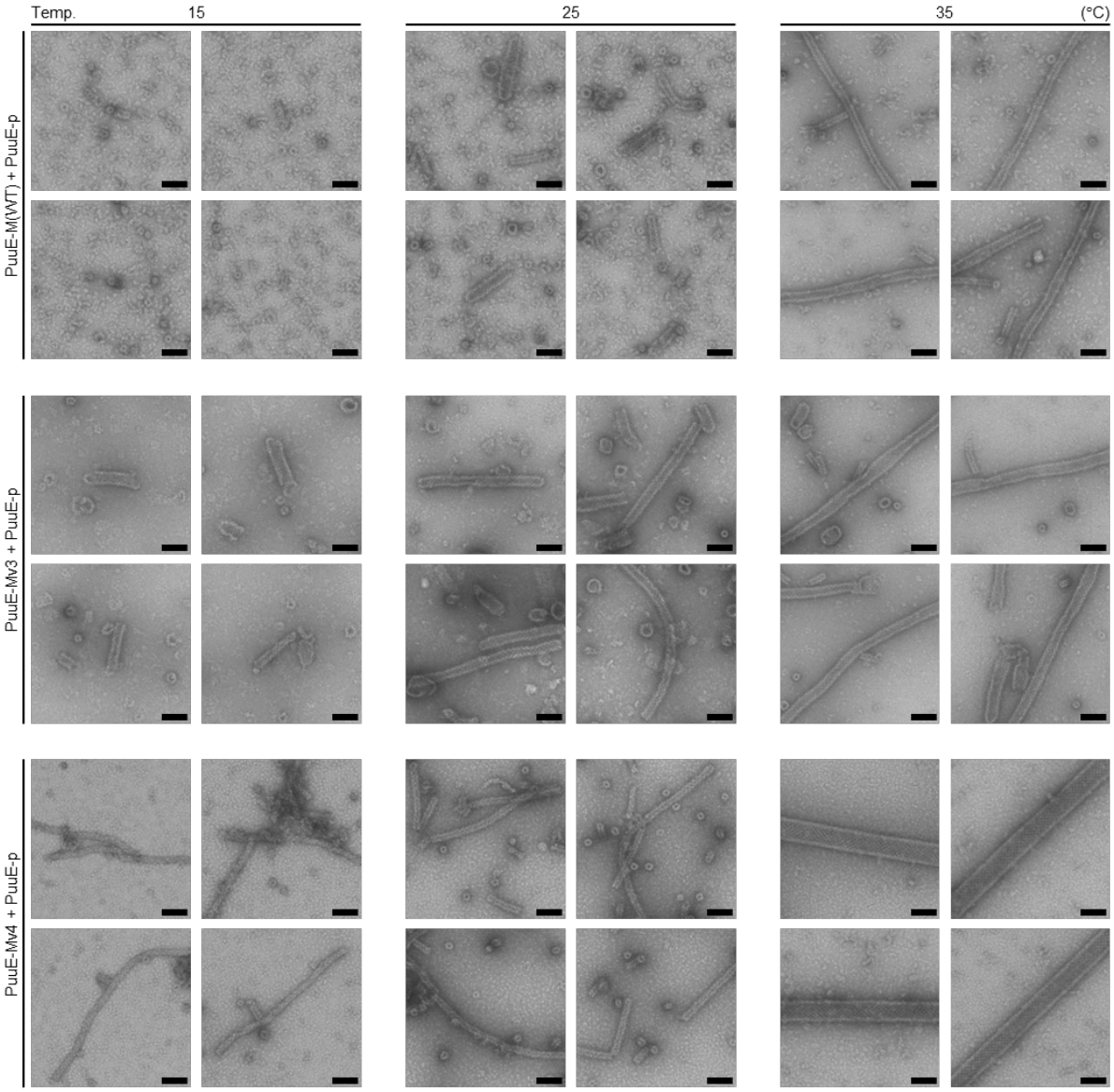

Supplementary Fig. 5. Additional nsTEM images corresponding to Fig. 3b. | Representative nsTEM images of tube formed from PuuE-M(WT) (top), PuuE-Mv3 (middle), and PuuE-Mv4 (bottom) mixed individually with PuuE-p and incubated for 24 h under the temperature conditions indicated at the top (15, 25, and 35 °C).

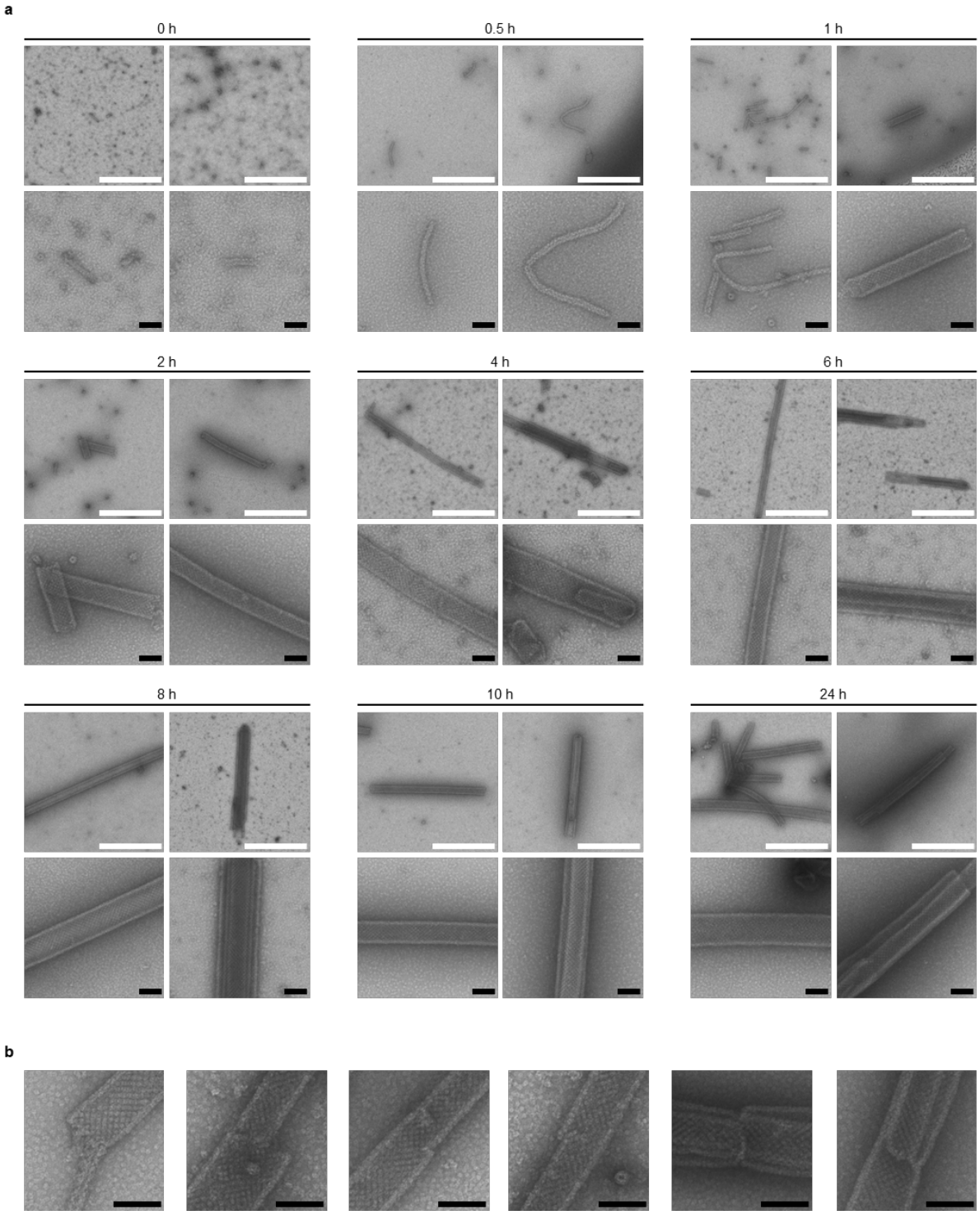

Supplementary Fig. 6. nsTEM analysis of PuuE-Mv4 tube formation at 35 °C. | a, Representative nsTEM images of tubes formed from PuuE-Mv4 mixed with PuuE-p and incubated at 35 °C from 0 to 24 h. These images provide time-course data complementary to Fig. 4, but show fields of view not included in the main figure. Time points are indicated at the top of each image. **b,** Representative nsTEM images

showing junctions between tubes of different diameters and displaced tube-wall segments, captured in the same dataset as panel **a**. Scale bars: 1 μm (white); 100 nm (black).

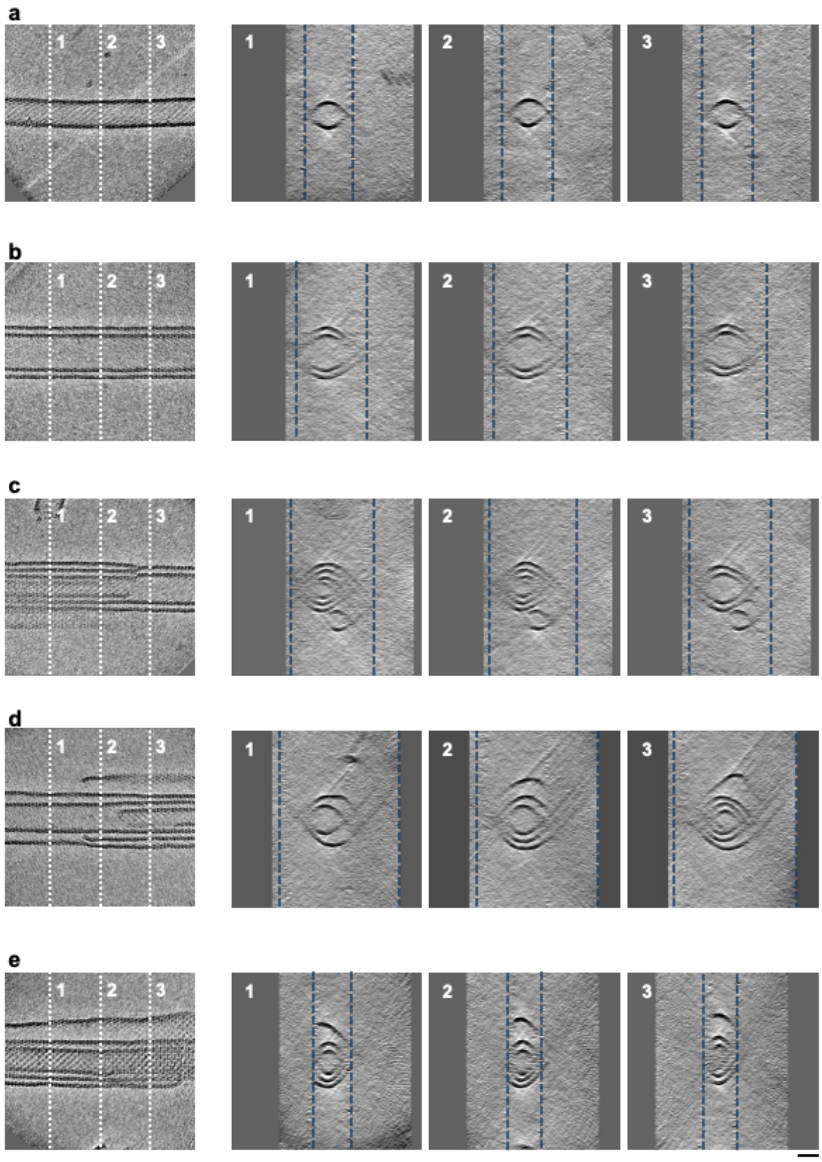

Supplementary Fig. 7. Cryo-ET analysis of PuuE-Mv4 tube formation at 35 °C. | a–d, Representative tomographic slices showing longitudinal views (left panel; single slice) and cross-sectional views (right panels; sum of 25 consecutive slices) of PuuE-Mv4 tubes in thicker ice (~120–280 nm) from cryo-ET reconstructions. Single- (a), double- (b), triple- (c), and four-layered (d) tubes are shown. **e**, PuuE-Mv4 tubes in ~80 nm of thin ice, showing pronounced tube flattening and an incomplete outer layer. White and blue dashed lines indicate the positions of cross-sections, labelled with numbers, and the ice surface, respectively. Scale bar: 50 nm.

Supplementary Tables

Name	Mutation	$\Delta\Delta G_{Pred}$ (kcal/mol)	T_m (°C)	$T_{m,Ave}$ (°C)
WT	None	None (= 0)	29.3 ± 1.7	31.7
			31.6 ± 1.0	
			34.1 ± 1.6	
Mv1	Q3Y	0.145	21.6 ± 5.8	-
			20.7 ± 13.3	
			−5.8 ± 48.9	
Mv2	P7G	0.489	40.1 ± 106.0	-
			−4.5 ± 134.0	
			25.8 ± 2.4	
Mv3	A14G	0.888	24.5 ± 1.1	25.5
			26.7 ± 1.4	
			25.3 ± 0.9	
Mv4	R16G	1.136	16.7 ± 2.8	17.2
			17.5 ± 4.2	
			17.5 ± 3.1	
Mv5	L28G	1.443	22.2 ± 1.6	22.6
			22.5 ± 1.0	
			23.1 ± 2.2	
Mv6	A20D	1.476	19.5 ± 1.8	-
			22.3 ± 4.7	
			19.5 ± 9.9	
Mv7	Q13D	1.546	17.6 ± 1.4	-
			−21.6 ± 93.1	
			14.9 ± 4.1	
Mv8	R21D	1.637	15.0 ± 3.2	17.7
			19.8 ± 2.2	
			18.2 ± 1.6	
Mv9	A27D	1.759	15.2 ± 6.4	-
			14.6 ± 3.3	
			9.7 ± 7.5	
Mv10	I10G	2.393	−5.6 ± 44.0	-
			−1.7 ± 34.8	
			16.7 ± 2.4	
Mv11	V5N	2.439	19.1 ± 3.2	20.9
			23.9 ± 1.4	
			19.8 ± 3.4	
Mv12	V17D	2.452	15.6 ± 4.2	-
			−11.3 ± 45.1	
			−4.6 ± 34.5	
Mv13	L24G	2.802	20.0 ± 4.4	-

			12.2 ± 7.5	
			26.5 ± 3.0	

Supplementary Table 1. M3L2(WT) and its mutants. | Predicted stability changes for point mutations ($\Delta\Delta G_{\mathrm{Pred}}$) derived from ThermoMPNN inference are shown for M3L2(WT) and its mutants (Mvs). T_{m} and $T_{\mathrm{m,Ave}}$ determined CD measurements are provided for coiled-coil complexes formed between p66α and each variant. T_{m} values are shown with standard deviation. Source data are provided as a Source Data file.

M3L2-Gly$_{50}$-p66α; M3L2-Gly$_{50}$-p66α
SGQLVTPADIRRQARRVKKARERLAKALQADRLAGGGGGGGGGGGGGGGGGGGGGGGGGGG
GGGGGGGGGGGGGGGGGGGGGGGPEERERMIKQLKEELRLEEAKLVLLKKLRQSQIQ

6xHis-TEVcs-M3L2(WT); 6xHis-TEVcs-M3L2
MHHHHHHENLYFQGSGQLVTPADIRRQARRVKKARERLAKALQADRLA

p66α; 6xHis-TEVcs-p66α
MHHHHHHENLYFQGPEERERMIKQLKEELRLEEAKLVLLKKLRQSQIQ

8xHis-TEVcs-M3L2(WT); 8xHis-TEVcs-M3L2
MHHHHHHHHENLYFQGSGQLVTPADIRRQARRVKKARERLAKALQADRLA

Mv1; 8xHis-TEVcs-M3L2(Q3Y)
MHHHHHHHHENLYFQGSGYLVTPADIRRQARRVKKARERLAKALQADRLA

Mv2; 8xHis-TEVcs-M3L2(P7G)
MHHHHHHHHENLYFQGSGQLVTGADIRRQARRVKKARERLAKALQADRLA

Mv3; 8xHis-TEVcs-M3L2(A14G)
MHHHHHHHHENLYFQGSGQLVTPADIRRQGRRVKKARERLAKALQADRLA

Mv4; 8xHis-TEVcs-M3L2(R16G)
MHHHHHHHHENLYFQGSGQLVTPADIRRQARGVKKARERLAKALQADRLA

Mv5; 8xHis-TEVcs-M3L2(L28G)
MHHHHHHHHENLYFQGSGQLVTPADIRRQARRVKKARERLAKAGQADRLA

Mv6; 8xHis-TEVcs-M3L2(A20D)
MHHHHHHHHENLYFQGSGQLVTPADIRRQARRVKKDRERLAKALQADRLA

Mv7; 8xHis-TEVcs-M3L2(Q13D)
MHHHHHHHHENLYFQGSGQLVTPADIRRDARRVKKARERLAKALQADRLA

Mv8; 8xHis-TEVcs-M3L2(R21D)
MHHHHHHHHENLYFQGSGQLVTPADIRRQARRVKKADERLAKALQADRLA

Mv9; 8xHis-TEVcs-M3L2(A27D)
MHHHHHHHHENLYFQGSGQLVTPADIRRQARRVKKARERLAKDLQADRLA

Mv10; 8xHis-TEVcs-M3L2(I10G)
MHHHHHHHHENLYFQGSGQLVTPADGRRQARRVKKARERLAKALQADRLA

Mv11; 8xHis-TEVcs-M3L2(V5N)
MHHHHHHHHENLYFQGSGQLNTPADIRRQARRVKKARERLAKALQADRLA

Mv12; 8xHis-TEVcs-M3L2(V17D)
MHHHHHHHHENLYFQGSGQLVTPADIRRQARRDKKARERLAKALQADRLA

Mv13; 8xHis-TEVcs-M3L2(L24G)
MHHHHHHHHENLYFQGSGQLVTPADIRRQARRVKKARERGAKALQADRLA

PuuE-M(WT); 6xHis-TEVcs-PuuE-M3L2
MHHHHHHENLYFQGVDYPRDLIGYGSNPPHPHWPGKARIALSFVLNYEEGGERNILHGDKESEA
FLSEMVSAQPLQGERNMSMESLYEYGSRAGVWRILKLFKAFDIPLTIFAVAMAAQRHPDVIRAMV
AAGHEICSHGYRWIDYQYMDEAQEREHMLEAIRILTELTGERPLGWYTGRTGPNTRRLVMEEGG
FLYDCDTYDDDLPYWEPNNPTGKPHLVIPYTLDTNDMRFTQVQGFNKGDDFFEYLKDAFDVLYA
EGAEAPKMLSIGLHCRLIGRPARLAALQRFIEYAKSHEQVWFTRRVDIARHWHATHPYTSGQLVT
PADIRRQARRVKKARERLAKALQADRLA

PuuE-p; 6xHis-TEVcs-PuuE-p66α
MHHHHHHENLYFQGVDYPRDLIGYGSNPPHPHWPGKARIALSFVLNYEEGGERNILHGDKESEA
FLSEMVSAQPLQGERNMSMESLYEYGSRAGVWRILKLFKAFDIPLTIFAVAMAAQRHPDVIRAMV
AAGHEICSHGYRWIDYQYMDEAQEREHMLEAIRILTELTGERPLGWYTGRTGPNTRRLVMEEGG
FLYDCDTYDDDLPYWEPNNPTGKPHLVIPYTLDTNDMRFTQVQGFNKGDDFFEYLKDAFDVLYA
EGAEAPKMLSIGLHCRLIGRPARLAALQRFIEYAKSHEQVWFTRRVDIARHWHATHPYTPEERER
MIKQLKEELRLEEAKLVLLKKLRQSQIQ

PuuE-Mv3; 6xHis-TEVcs-PuuE-M3L2(A14G)
MHHHHHHENLYFQGVDYPRDLIGYGSNPPHPHWPGKARIALSFVLNYEEGGERNILHGDKESEA
FLSEMVSAQPLQGERNMSMESLYEYGSRAGVWRILKLFKAFDIPLTIFAVAMAAQRHPDVIRAMV
AAGHEICSHGYRWIDYQYMDEAQEREHMLEAIRILTELTGERPLGWYTGRTGPNTRRLVMEEGG
FLYDCDTYDDDLPYWEPNNPTGKPHLVIPYTLDTNDMRFTQVQGFNKGDDFFEYLKDAFDVLYA
EGAEAPKMLSIGLHCRLIGRPARLAALQRFIEYAKSHEQVWFTRRVDIARHWHATHPYTSGQLVT
PADIRRQGRRVKKARERLAKALQADRLA

PuuE-Mv4; 6xHis-TEVcs-PuuE-M3L2(R16G)
MHHHHHHENLYFQGVDYPRDLIGYGSNPPHPHWPGKARIALSFVLNYEEGGERNILHGDKESEA
FLSEMVSAQPLQGERNMSMESLYEYGSRAGVWRILKLFKAFDIPLTIFAVAMAAQRHPDVIRAMV
AAGHEICSHGYRWIDYQYMDEAQEREHMLEAIRILTELTGERPLGWYTGRTGPNTRRLVMEEGG
FLYDCDTYDDDLPYWEPNNPTGKPHLVIPYTLDTNDMRFTQVQGFNKGDDFFEYLKDAFDVLYA
EGAEAPKMLSIGLHCRLIGRPARLAALQRFIEYAKSHEQVWFTRRVDIARHWHATHPYTSGQLVT
PADIRRQARGVKKARERLAKALQADRLA

Supplementary Table 2. Amino acid sequences of the protein constructs used in this study.